ADVANCED ENERGY MATERIALS
www.advenergymat.de

Scalable, Light Rechargeable Energy Storage Based on Osmotic Effects and Photochemical Reactions in a Hair-Thin Filament

*Puguang Peng, Han Qian, Feiyao Yang, and Di Wei**

Scalable high-performance distributed energy management systems (DERMS) on one micron-scale fiber pose significant challenges. Here, an ultrafine single filamentary iontronic power source (10 µm thickness) is presented that utilizes ion transport within graphene oxide (GO) nanoconfined channels and silver halide interfacial redox reactions to achieve impressive gravimetric power (884.95 W kg^{-1}) and energy densities (108.7 Wh kg^{-1}), alongside rapid photo-recharging capabilities within seconds. The controlled ultrasonic spraying technique enables the seamless integration of stable GO channels on filaments, preserving the integrity of other active layers. Through a detailed investigation of ion dynamics, an electrochemical nanoconfined ion transport pathway is proposed, demonstrating the polarization resistance of the filament battery is stable over a certain length, facilitating scalability. These devices exhibit consistent performance across a wide temperature range and under various environmental conditions, maintaining stability after 10 000 bending cycles. The world's thinnest rechargeable filament battery, with a total diameter of ≈120 µm is reported, offering a promising solution for next-generation smart textiles, microelectronic circuits, and wearable DERMS.

1. Introduction

The increasing demand for sustainable and decentralized energy solutions has driven significant progress in distributed energy management systems (DERMS), which are essential for optimizing the integration and utilization of energy storage and harvesting.[1] In recent years, significant progress has been made in flexible, lightweight, and scalable energy storage technologies, with fiber-based batteries and capacitors, gaining attention as promising solutions for distributed systems.[2] These devices offer distinct advantages, including mechanical flexibility, seamless integration into textiles and wearables, and the potential to be woven into complex electronic systems. As the demand for higher energy density, space efficiency, and multifunctionality in electronics increases, future developments are expected to shift toward even more miniaturized filamentary structures (**Figure 1a**). Such advancements would enable enhanced performance in compact spaces, supporting the evolution of smart textiles,[3] implantable medical fibers,[4] and next-generation flexible micro-integrated circuits,[5] where size constraints and scalability are critical for widespread adoption. Additionally, fiber-based energy harvesters, including integrated solar cells,[6] triboelectric nanogenerators (TENGs), piezoelectric devices,[7] and humidity-driven osmotic power systems,[8] offer a continuous power supply by capturing ambient energy. The integration of energy harvesting with storage facilitates the development of DERMS on a single filament, effectively addressing the growing demand for mobile distributed energy solutions. However, achieving this integration presents critical challenges, such as optimizing energy conversion efficiencies, maintaining operational stability under various operational conditions, and ensuring consistent performance while minimizing the device for practical scalability.

Energy storage is crucial for the development of filamentary DERMS. Existing fiber-based energy storage technologies include supercapacitors,[9] lithium-ion batteries (LIBs),[10] lithium-sulfur batteries,[11] sodium-ion batteries,[12] calcium-oxygen batteries,[13] silicon-oxygen batteries,[14] and various metal-air batteries.[15] Of these, fiber-based supercapacitors (FSC) and LIBs have garnered the most attention. One of the first FSC with the twisted carbon-nanotubes (CNTs) was reported in 2003,[9b] and it took nearly a decade for the development of a coaxial ultrafine supercapacitor, with a diameter of≈20 µm.[9a] The evolution of fiber-based LIBs began ≈2012, when LG Chem introduced a cable-type LIBs based on hollow multi-helix electrodes.[16] After that, fiber-based LIBs evolved from cable to twisted structures, due to the latter's reduced internal resistance and the rapid continuous

P. Peng, H. Qian, F. Yang, D. Wei
Beijing Institute of Nanoenergy and Nanosystems
Chinese Academy of Sciences
Beijing 101400, P. R. China
E-mail: dw344@cam.ac.uk
P. Peng, H. Qian
School of Nanoscience and Engineering
University of Chinese Academy of Sciences
Beijing 100049, P. R. China
D. Wei
Centre for Photonic Devices and Sensors
University of Cambridge
9 JJ Thomson Avenue, Cambridge CB3 0FA, UK

The ORCID identification number(s) for the author(s) of this article can be found under https://doi.org/10.1002/aenm.202405547

DOI: 10.1002/aenm.202405547

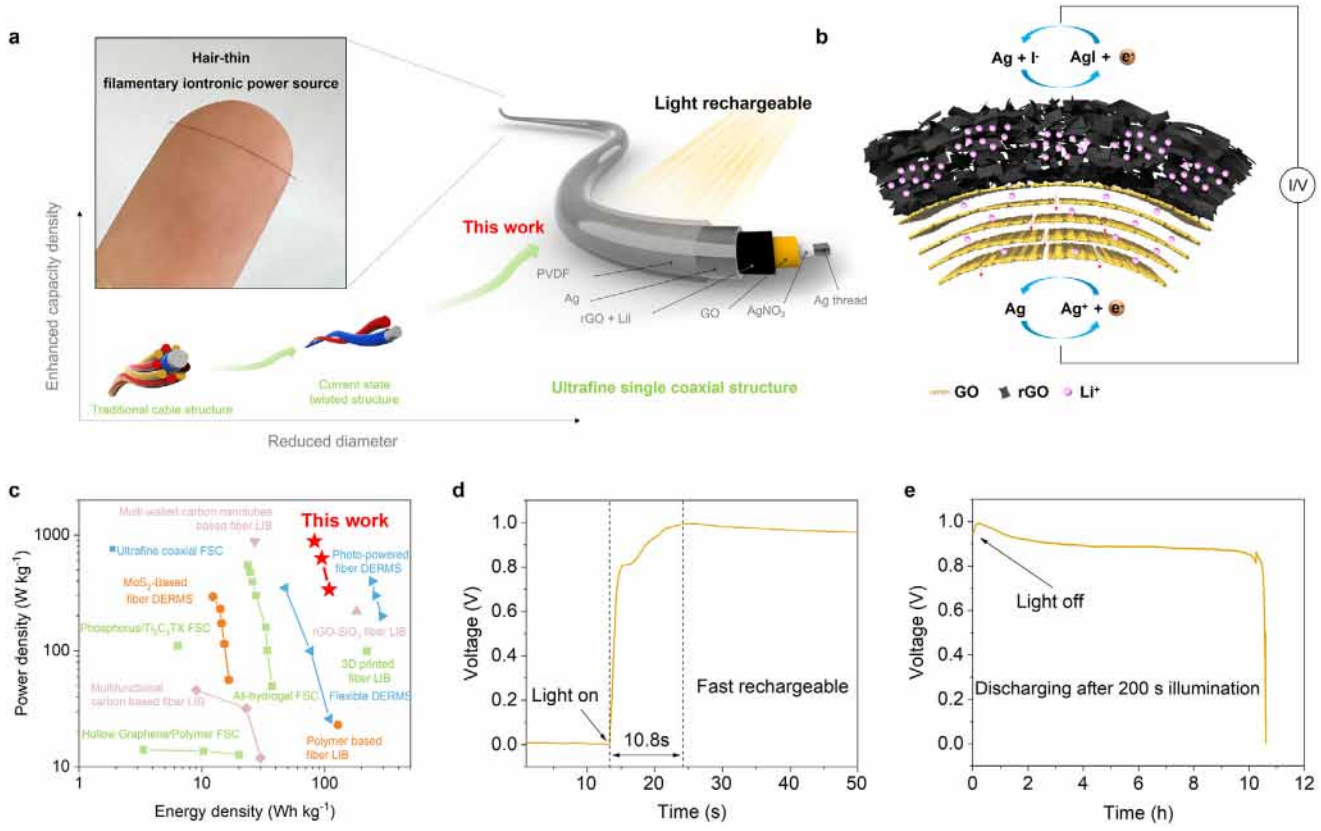

Figure 1. Hair-thin filamentary iontronic power source. a) Graphical illustration showing the evolution of structures and the reducing diameter for fiber batteries. Filamentary iontronic power source with ultrafine coaxial structure can reach the thinnest diameter compared with traditional cable and twisted structures. Photograph showing the hair-thin filament battery, demonstrating its microscale dimension comparable to a human hair. b) Schematic illustration of the light-rechargeable filament, which consists of a filamentary Ag core, $AgNO_3$ layer, GO, and rGO layer with embedded Li^+ ions. The system operates via silver halide (Ag/AgI) interfacial redox reactions driven by ion transport across the GO layer, enabling efficient energy harvesting and storage. c) Ragone plot comparing the power density and energy density of the filament battery (red star) with various fiber-based energy harvesting and storage technologies. Data from Table S1(Supporting Information). d) Open circuit voltage test showing the fast rechargeability of the filament battery, achieving full voltage charging in just 10.8 s under illumination. e) Discharge profile of the filament battery at 1 μA following 200 s of illumination, demonstrating stable output for over 10 h post-photo -recharging.

fabrication, and such twisted structure also leads to the development of various fiber-based batteries as mentioned above.[2b] However, the requirement for tightly twisted electrodes leads to increased thickness and weight, limiting miniaturization potential and lowering energy density. There is a consensus in the field that fiber-based batteries should incorporate finer coaxial structures to improve performance and flexibility for future applications. Additionally, a coaxial design with asymmetric electrode areas may provide benefits in equalizing current distribution and minimizing ion polarization, leveraging the ionic axial transport pathway. Although some coaxial fiber batteries exist, it has been observed that devices fabricated without twisting often suffer from low structural integrity, limiting their practical application.[2a] This issue likely stems from common fabrication methods involving liquid environments, such as spinning, coating, and deposition, which lead to undesirable interactions between successive layers on a single filament.[2c] As a result, no practical, scalable, ultrafine filament-based battery with a coaxial structure has been reported to date. Additionally, the high charging voltage thresholds of current energy storage systems complicate their direct integration with energy harvesting technologies for DERMS, frequently necessitating tandem devices for autonomous recharging.[17] These fabrication, structural, and operational limitations, coupled with safety concerns, underscore the need for alternative approaches. Our strategy, leveraging ultrafine filamentary iontronic power sources based on the osmotic effect, overcomes these challenges. By employing elongated, micron-scale filaments, we reduce thickness and enhance flexibility without sacrificing performance. Moreover, our system seamlessly integrates with energy harvesting technologies, synergizing electrochemistry and photochemistry via photo-sensitive AgI. This enables direct, rapid charging of the iontronic power source, offering an efficient, flexible, and compact solution for next-generation DERMS applications.

The osmotic effect of ions efficiently converts Gibbs free energy into electrical energy through directional ion diffusion, enabled by highly selective and efficient ion transport channels.[18] Nanoconfined iontronics harnessing osmotic effects utilize enhanced ion dynamics within electrochemical systems, seamlessly integrating the characteristics of electrochemical energy storage with salinity gradient energy harvesting.[19] The fully printable nanoconfined iontronic power sources present distinct

advantages, including their ultra-thin micro-scale dimensions and improved safety profiles.[20] These systems exhibit pronounced anomalous ion dynamics, especially within nanoconfined channels measuring less than 100 nm in diameter, where electrostatic forces within electrical double layers (EDLs) significantly enhance ion transport.[21] A major challenge in advancing iontronic filamentary DERMS is the creation of stable, extended nanoconfined channels along the filament. While the internal polarization resistance of fiber batteries has been shown to follow a hyperbolic cotangent relationship with fiber length,[10b] competition between horizontal and vertical ion transport in long-distance nanoconfined channels may arise. Understanding this interplay in the context of ion dynamics is critical for developing scalable, rechargeable iontronic filamentary DERMS. Graphene oxide (GO), a widely used 2D material in energy harvesting,[22] ionic gating,[23] and ionic logic units,[24] provides a promising platform for examining ion dynamics in nanoconfined spaces. GO's negatively charged functional groups enable rapid cation transport within its nanoconfined channels.[18] The incorporation of well-aligned GO nanochannels on filaments could revolutionize iontronic energy storage, enabling scalable, rechargeable, and environmentally sustainable technologies.

In this work, we introduce the world's thinnest rechargeable filamentary iontronic power source, with a total diameter of ≈120 µm and a battery thickness of just 10 µm, designed for DERMS. This ultrafine filament harnesses ion transport within GO nanoconfined channels and silver halide interfacial redox reactions to achieve remarkable gravimetric power and energy densities of 884.95 W kg^{-1} and 108.7 Wh kg^{-1}, respectively, surpassing most fiber-based energy storage and harvesting devices (Figure 1b,c). By utilizing ultrasonic spray-coating technology, stable and extended nanoconfined channels were constructed on the filaments, ensuring that each layer remains unaffected, facilitating scalability. Both experimental and theoretical analyses have confirmed that the internal polarization resistance of these long filament batteries decreases initially and then stabilizes as the length increases. COMSOL dynamic simulation proposed an electrochemical-driven ion diffusion model, wherein ion transport pathways are nanoconfined to each specific unit regions by the internal electrochemical field, potentially explaining the stable resistance observed. Additionally, reversible photochemical reactions enable rapid photo-recharging, with the device recovering 99% of its voltage in just 10.8 s, achieving a photo-recharging efficiency of up to 100% (Figure 1d,e). At a cost of under US$0.02 per meter, this scalable technology can be seamlessly integrated into everyday textiles, providing a cost-effective, high-performance solution for powering electronic devices and real-time health monitoring systems in next-generation smart textiles and wearable DERMS.

2. Results and Discussion

2.1. Mechanism of the Rechargeable Filament Battery

The essence of nanoconfined iontronics resides in the meticulous regulation of ions via both physical and chemical methodologies. For instance, the reverse electrodialysis (RED) system, through electrode redox reactions, facilitates the direct extraction of electrical energy from ionic salinity gradients.[25] To elucidate the fundamental mechanisms governing filament battery, a planar device was initially constructed, enabling the direct observation of ion dynamics and interfacial redox reaction processes, as illustrated in **Figure 2**a. Two silver electrodes were initially screen-printed onto a PET substrate. Subsequently, an ultrasonic spray system was employed to coat GO/$AgNO_3$ and GO inks onto one side of the Ag electrode, which was then dried to form the cathode side. Similarly, LiI-reduced graphene oxide (rGO) ink was applied to the other Ag electrode as the anode side, overlapping with the GO film to construct the planar Ag/$AgNO_3$-GO/LiI-rGO/Ag iontronic device. In our design, GO serves as the nanoconfined cation channels (Figure S1, Supporting Information), enabling efficient Li^+ transport between the anode and cathode, thereby generating osmotic effect. Silver ions (Ag^+) in $AgNO_3$ at the cathodic side are reduced, while the Ag electrode on the anodic side undergoes oxidation, forming silver iodide (AgI) by compositing with the remaining iodide ions. The coupling of osmotic effect and redox reactions in iontronics can yield substantial energy and power outputs.[20e,25b] Compared to other halogens like chlorine and bromine, iodine's interaction with silver yields the lowest standard electrode potential (relative to normal hydrogen electrode, NHE), enabling the device to achieve a relatively higher redox potential (Figure S2, Supporting Information). Molecular dynamics simulations have demonstrated that within GO nanochannels, the migration rate of dehydrated alkali metal ions follows the order of $Li^+ > Na^+ > K^+$.[20e] This may be due to Li^+ possessing the most compact structure and the lightest mass among the three alkali metal ions. Hence, Li^+ were selected as the charge carriers in this study. For the Ag/$AgNO_3$-GO/LiI-rGO/Ag planar iontronic device, X-ray diffraction (XRD, Figure 2b) revealed an increase in the interlayer spacing of GO from 7.558 to 7.9361 Å after discharge, which may be attributed to the migration of Li^+ from the anode side to the cathode side. The intercalation of Li^+ led to an expansion of the GO interlayer spacing. Inductively coupled plasma mass spectrometry (ICP-MS, Figure 2c) clearly showed that the lithium-ion concentration in the GO side increased from 432 to 24365 ppm after discharging, further confirming the direct diffusion of lithium ions from the LiI-rGO side to GO. Additionally, Raman spectroscopy (Figure 2d) detected an increase in the I_D/I_G ratio (from 1.071 to 1.136) on the GO side after discharging, suggesting that Li^+ insertion into the GO layers introduces more defects. Further detailed X-ray Photoelectron Spectroscopy (XPS, Figure 2e) of lithium revealed a prominent peak at 55.7 eV on the GO side after discharging, which is attributed to Li-N bonds. This may be associated with some lithium ions replacing Ag^+ within the $AgNO_3$ lattice after transmission through the GO, ultimately leading to the formation of $LiNO_3$. This phenomenon has been previously validated using density functional theory (DFT) energetic calculations.[18] On the rGO side, the formation of AgI after discharging was directly confirmed by XRD as shown in Figure 2f. The working process of the planar iontronic device was further observed through optical microscopy (Figure S3, Supporting Information), where silver nitrate particles on the cathode side were visibly transformed into metallic silver particles after discharging. At the interface between rGO and the Ag electrode on the anode side, white crystalline salts formed, which were further identified as AgI via EDS analysis, confirming a 1:1 ratio of silver to iodine, as shown in Figure S4 (Supporting Information). This

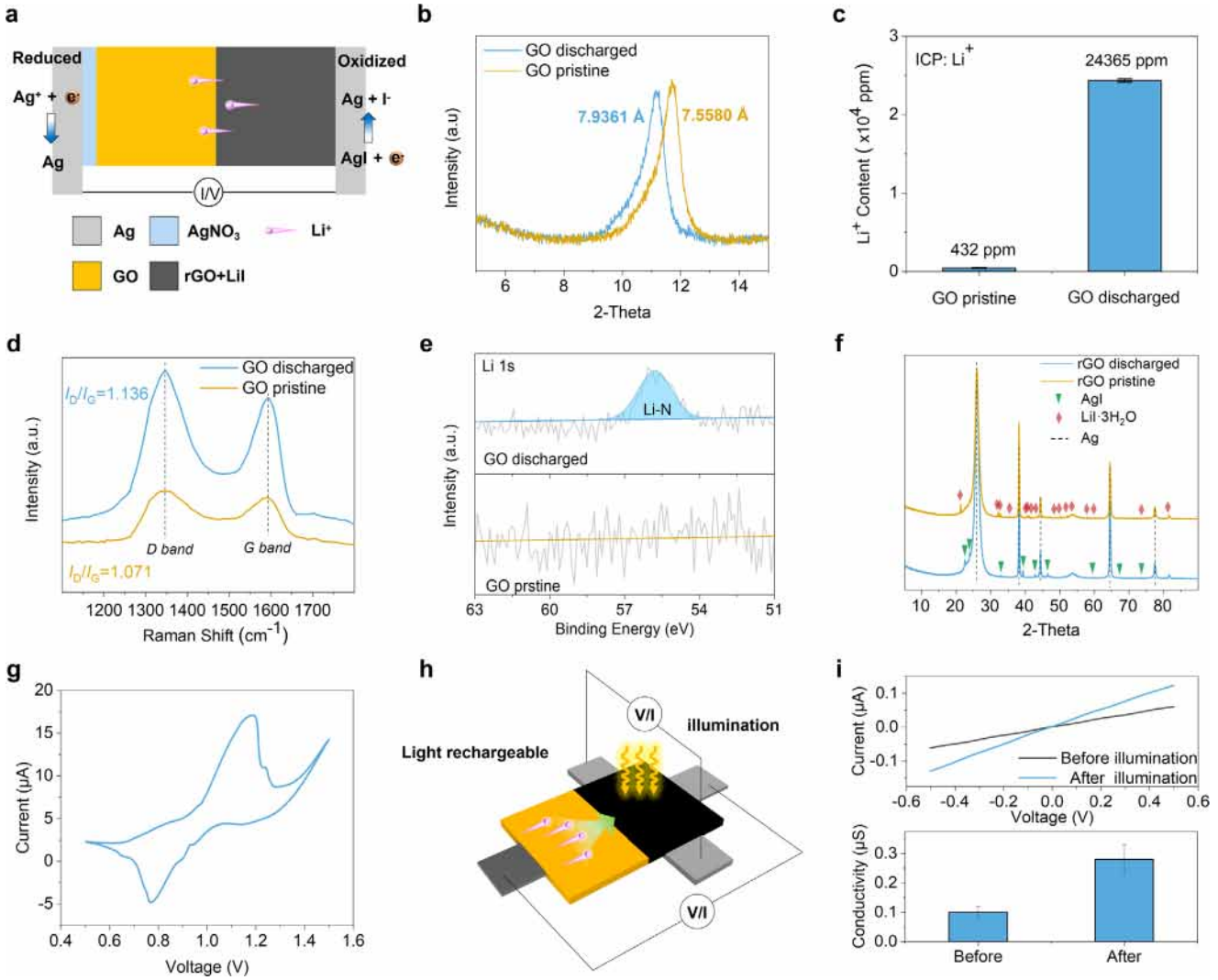

Figure 2. Discharging and photo-recharging mechanism of the filament battery. a) Schematic mechanism of the planner iontronic power source. b) X-ray diffraction (XRD) patterns of GO in pristine and discharged states. c) Inductively coupled plasma (ICP) analysis demonstrating significant Li^+ content in the discharged GO (24 365 ppm) compared to the pristine GO (432 ppm), confirming effective ion transport. d) Raman spectra comparing discharged and pristine GO, with a slight increase in the I_D/I_G intensity ratio from 1.071 to 1.136 after discharge. e) X-ray photoelectron spectroscopy (XPS) of Li 1s peaks for GO, indicating the presence of Li-N bonding in the discharged state. f) XRD patterns of rGO in discharged and pristine states, revealing the formation of AgI after discharging. g) Cyclic voltammetry (CV) curve displaying typical redox peaks, indicating the reversible electrochemical behavior of the iontronic power source. h) Schematic of the home-made four electrode system for photo-rechargeable iontronics, where ions can migrate back to rGO side under the photo electrochemical built-in electric field. i) *I–V* test of rGO side before and after illumination, showing improved conductivity of rGO after illumination, confirming the ions migrating back. The width of the rGO is 5 mm.

ion diffusion and interfacial redox reaction process were found to be reversible, as evidenced by the cyclic voltammetry (CV) test in Figure 2g, which displayed nearly symmetric redox peaks.

In this design, the generated AgI can be directly used to form the DERMS without introducing additional components, owing to its photosensitive decomposition properties. Silver halides have historically been employed in photosensitive applications such as camera films, photochromic glasses[26] and photocatalysis.[27] The photochemical decomposition of silver halides generates photoelectrons while retaining halogen ions, making it highly suitable for our iontronic system to regulate the ionic-electronic interface via light. Light-driven ion migration plays a pivotal role in the photo-recharging process. Our approach offers a distinct advantage comparing with existing light-driven ionic pumps,[28] photochemical ionic switches,[29] and organic photoelectrochemical ionic diodes,[30] as it eliminates the need for additional fabrications or complex architectures. This simplicity makes it more practical to integrate DERMS within a micron-scale filament. Thus, light can be directly harnessed to rapidly recharge the iontronics by converting solar energy into storable chemical energy, providing an efficient and decentralized solution for energy harvesting. Upon exposure to ultraviolet light (UV, 365 nm, 350 mW cm^{-2}), the voltage of the fully discharged device rapidly restored to 1 V, as shown in Figure S5 (Supporting Information). A gradual decline in voltage was also observed with extended illumination time. This decline can

be attributed to the reduction in ionic conductivity on the rGO side, caused by the back-migration of lithium ions. This phenomenon was measured using a custom-made four-electrode system (Figure 2h,i, where the ionic conductivity on the rGO side increased from 0.22 μS cm^{-1} before photo-recharging to 0.54 μS cm^{-1} after. Remarkably, the device was able to sustain discharge for over 10 h following photo-recharging, demonstrating the practicality of using light for extended energy release. We have also tested the photo-recharging performance under visible light with various intensities, showing the similar photo-recharging behavior compared to UV light, with a maximum solar-to-output electricity efficiency (SOEE) of 2.5% for UV light, and 2.12% for visible light (Figure S6, Supporting Information). The underlying mechanism of this photo-recharging process is depicted schematically in Figure S7 (Supporting Information). Upon illumination, the photon energy facilitates the transition of electrons from the valence band (VB) to the conduction band (CB) within the AgI crystals, generating photogenerated electron/hole pairs.[17a,27,31] This process establishes a photo induced built-in electric field, which in turn drives the reversible transport of lithium ions from GO to rGO. The photogenerated electron/hole pairs can also trigger the reduction of silver ions in AgI crystals, releasing iodide ions ($AgI + e^-_{h\nu} \rightarrow Ag + I^-$). The prerequisites for photochemical reactions can be explained by the matched bandgap energy levels with redox potentials,[32] as illustrated in Figures S8 and S9 (Supporting Information). The bandgap structure of AgI was determined via UV–vis diffuse reflectance spectroscopy and XPS. AgI exhibits a bandgap energy of 2.69 eV, with a VB energy level at 0.83 eV and a predicted CB energy level at −1.86 eV. The oxidation potential is positioned above the VB, while the reduction potential lies below the CB, ensuring that photogenerated electrons can effectively induce the decomposition of AgI without significant energy barriers.

2.2. Fabrication of the Filament Battery

Building upon the aforementioned components and mechanisms, we have fabricated a hair-thin filamentary iontronic power source on a single filament. A primary challenge in developing such filaments was ensuring the uniform and stable deposition of active materials on the filamentary electrode. Previous methods predominantly relied on slurry coating,[10b] which often resulted in uneven coating due to the additional Laplace surface tension on the curved fiber surface (Figure S10, Supporting Information). Herein, we employed an in situ synthesis coupled with ultrasonic spray deposition techniques, facilitating the scalable fabrication of stable filamentary iontronic power sources, as illustrated in **Figure 3**a. Optical photos of each fabrication stage on the filament are provided in Figure S11 (Supporting Information). Initially, a conductive silver filament was fully immersed in a HNO_3 mist, allowing for the in situ formation of an $AgNO_3$ active material coating. Through detailed studies, we determined that a treatment duration of 10 min provided an optimal balance between $AgNO_3$ active material thickness and electrode impedance, thereby promoting favorable ion diffusion dynamics at the interface (Figures S12 and S13, Supporting Information). Subsequently, a customized industrial ultrasonic spray deposition system was employed to construct the GO-based nanoconfined channels on the filament (Figure 3b; Video S1, Supporting Information). The GO ink, with 10% wt Nafion, was uniformly sprayed onto the filament continuously. The inclusion of Nafion ensured the integrity of the GO coating (Figure S14, Supporting Information) and maintained its cationic selectivity.[33] The infrared heating plate positioned behind the spray nozzle facilitated rapid drying of the GO droplets and their stable adhesion to the filament without compromising the underlying $AgNO_3$ layer. In accordance with the Sauter diameter principle, droplet size is contingent upon the equilibrium between viscosity and spray pressure.[34] By modulating the viscosity of the GO ink (Figure 3c) and the spray pressure (Figure 3d) to regulate GO droplet size, we can effectively minimize drying time and optimize the loading thickness of the GO film on the filament. The GO surface, rich in oxygen-containing functional groups, created nanoconfined channels that facilitated cation transport. A typical 5 μm thickness GO nanoconfined channel constructed on the filament is shown in Figure 3e. The stability and cationic conductivity of the 5 μm GO film were found to be optimal when tested in a customized device (Figure S15, Supporting Information). Importantly, the GO thickness remained consistent along a 50 cm length of the filament after spraying (Figure 3f). Even under bending conditions, the GO coating on the filamentary surface exhibited no significant delamination or cracking (Figure 3g). In the same way, we continued to spray the LiI-rGO to form an ion storage layer. The thickness of the LiI-rGO layer closely matched that of the GO layer, achieving a near 1:1 capacity matching ratio, which is crucial for high-performance electrochemical storage units due to its impact on ion diffusion.[35] Finally, a silver paste was applied to complete the outer layer of the filament battery. This spray-drying fabrication process is scalable, as evidenced by the production of varying lengths of the filament battery (Figure S16, Supporting Information). The resulting filament battery had diameters of ≈120 μm (Figure 3h, inside the encapsulated tube), with potential reductions to a few microns given sufficiently fine metal wires. Elemental mapping of the obtained filament battery (Figure 3i–m) revealed a sandwich overlapped structure of the characteristic elements within each component. The rapid spray-drying process effectively prevented interlayer interference, maintaining structural integrity without visible damage. The unencapsulated filament battery demonstrated a stable open-circuit voltage (Voc) of ≈1 V over 100 h in ambient environment of Beijing, 25.0 °C and 15.0%–20.0% RH, as shown in Figure S17 (Supporting Information). This stability likely results from the low humidity, which hinders ion transport within the GO nanoconfined channels, allowing the Voc to remain stable over extended periods.[18,20a,e] The filament battery can also be encapsulated within a Polyvinylidene fluoride (PVDF) shrinkable tube and tested for electrochemical performance after the injection of room-temperature ionic liquids (RTILs). RTILs can serve as a switch to activate the filament battery, preventing self-discharge. Due to their non-flammability, electrochemical and thermal stability, RTILs have been reported as effective media for accelerating ion transport in the nanoconfined channels.[36] The encapsulated filament battery exhibited excellent waterproof performance, maintaining stable voltage output after immersion in water for one week (Figure S18, Supporting Information). Additionally, due to the ultrafine structure and scalable spray fabrication process, our filament battery possesses a distinct cost

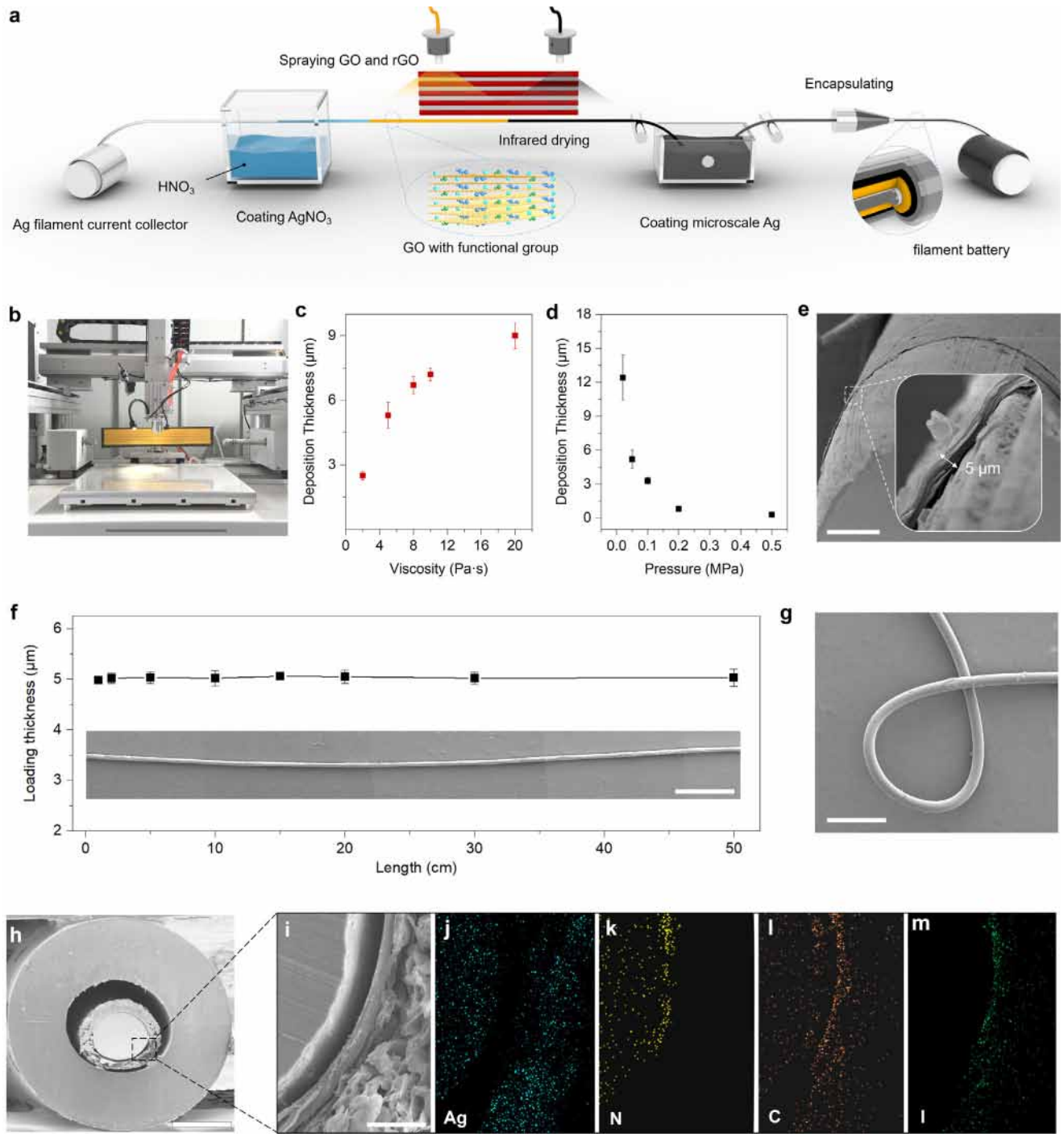

Figure 3. Fabrication process of the stable GO-based filament battery a) Schematic illustration of the fabrication process for filament battery. The process involves coating a filamentary silver current collector with $AgNO_3$ by HNO_3 mist, followed by spraying GO and rGO layers with infrared drying, encapsulation, and the final filament battery structure. b) Image of the automated ultrasonic spraying device used for coating GO and rGO, showing the precision and scalability of the process. c) Plot of deposition thickness as a function of viscosity, demonstrating a positive correlation between the viscosity of the GO slurry and the thickness of the deposited layer. d) Plot of deposition thickness as a function of pressure, showing the inverse relationship between spray pressure and coating thickness. e) Scanning electron microscope (SEM) image of the cross-section of the coated filament, revealing the uniformity of the GO layer around the Ag core. Scalar bar 25 μm. f) Thickness measurement along the length of the coated filament, indicating consistent coating thickness over 50 cm. The inset shows a magnified SEM image of the coated filament surface. Scalar bar, 1 mm. g) SEM image of the flexible and bendable filament battery, highlighting its potential for integration into wearable textiles. Scalar bar 500 μm. h) SEM image of a cross-section of the encapsulated filament battery. Scalar bar 100 μm. i–m) Elemental mapping of the corresponding cross-sectional SEM image, showing the separate distribution of (j) silver, (k) nitrogen, (l) carbon, and (m) iodine in each layer. Scalar bar 20 μm.

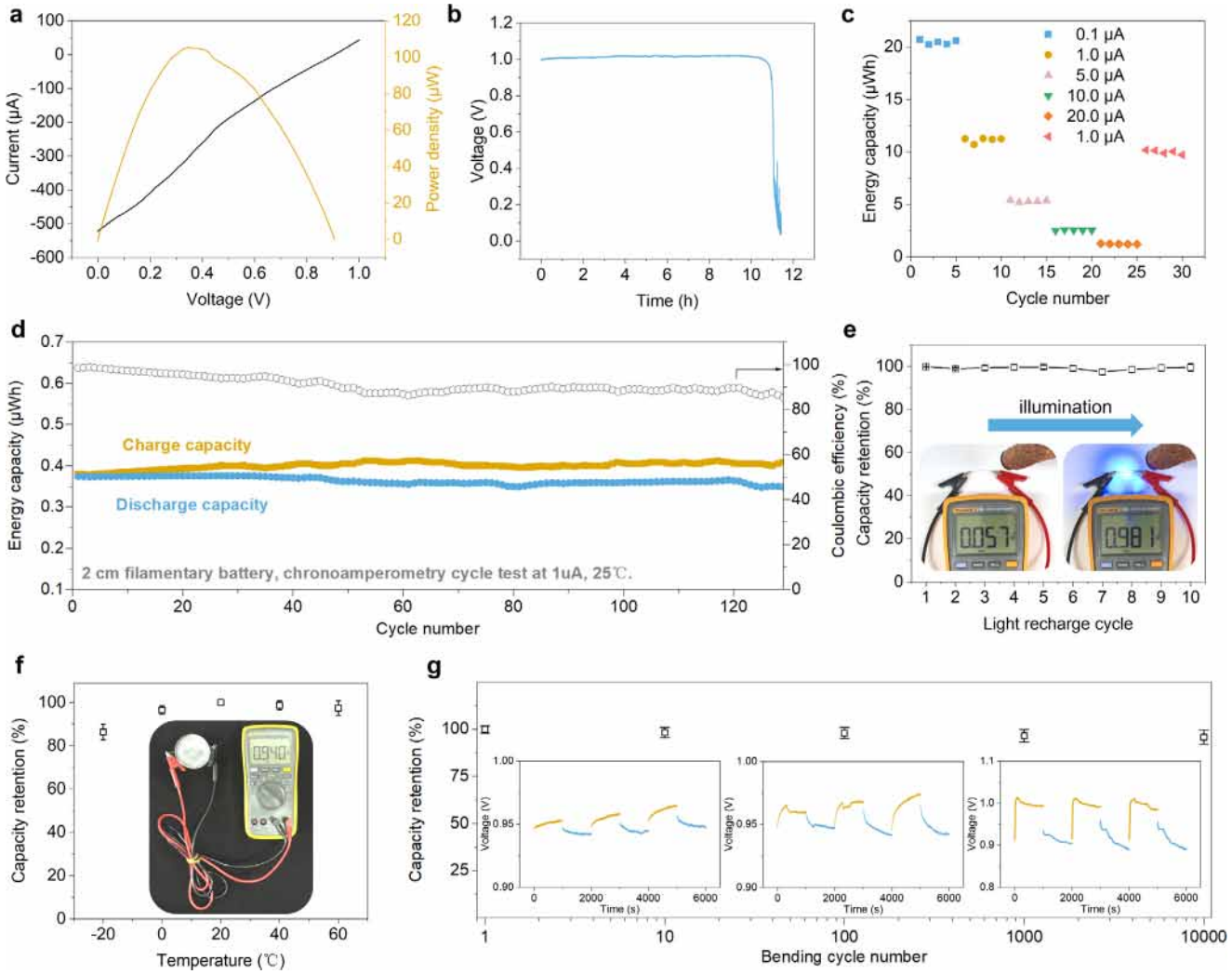

Figure 4. Electrochemical performance and stability of the filament battery a) I-V curve with corresponding power capacity, demonstrating a peak power ≈113 μW within 2 cm filament battery. b) Chronoamperometric discharge profile showing stable output over 12 h. c) Energy capacity under different discharge currents, showcasing the device's stability across various operational currents. d) Cycling stability at a 1 μA current for over 120 cycles, with consistent charge/discharge capacities. e) Photo rechargeability test under illumination, showing nearly full capacity retention after repeated light exposure cycles. Inset photo shows the recovered voltage after illumination. f) Capacity retention across a broad temperature range, from −20 to 60 °C, confirming the device's environmental resilience. Inset photo shows the stable voltage under freezing. g) Bending tests over 10000 cycles with voltage retention, highlighting the mechanical robustness of the flexible filament battery.

advantage, priced at only 0.0158 USD m^{-1} (Table S2, Supporting Information), making them suitable for large-scale applications in textile electronics and wearable distributed energy management systems.

2.3. Electrochemical Performance and Scalability of the Filament Battery

The exceptional power capability of the filament battery is demonstrated firstly by linear voltammetric test. With a single 2 cm long unit, the short-circuit current (Isc) of the filament battery can reach≈530 μA and the maximum power capability is ≈113 μW (**Figure** 4a). When discharged at a current of 1 μA, the energy capacity of the filament battery reaches 11.235 μWh (Figure 4b). Further evaluation of the capacity retention of the filament battery at various discharge rates (Figure 4c) revealed that, even at a discharge current of 20 μA, the energy of the filament battery remained at 1.223 μWh. When the discharge current was restored to 1 μA, the energy capacity rebounded to 10.762 μWh. This high-power density and excellent rate performance underscore the rapid charge-discharge capability of the filament battery, which can be attributed to the ultrathin GO film, effectively shortening the ion transport pathway. In addition, the filament battery also exhibited remarkable cycle stability. After 125 galvanostatic charge-discharge (GCD) cycles, the capacity retention remained at 95.6%, with a Coulombic efficiency of 89.5% (Figure 4d). The individual GCD curves for the first to the 20th cycles are shown in Figure S19 (Supporting Information). The discharge voltage of the filament remained almost constant at 0.95 V, while the

charging voltage plateau showed a slight increase, which may be attributed to ionic polarization at the electrode interface after cycles. The filament battery also demonstrated promising photo-recharging cycle stability. As shown in Figure 4e and Video S2 (Supporting Information), the filament battery maintained 98% capacity retention over ten photo-recharging and discharging cycles. Moreover, due to the injection of RTIL, our filament battery operated over a wide temperature range of −20–60 °C, with capacity retentions exceeding 80% at −20 °C and 90% at 60 °C (Figure 4f). Embedded photographs illustrate that even when the filament battery was frozen inside ice, it maintained a stable voltage output of 0.94 V. The broad environmental adaptability and photo-recharging capability of the filament battery make it particularly suitable for outdoor applications. Additionally, the encapsulated filament battery exhibited enhanced flexibility and durability, capable of a strain of up to 12% (Figure S20a, Supporting Information). Even under dynamic bending conditions (with a curvature radius of 1 cm), the filament battery could maintain a stable voltage output (Figure S20b and Video S3, Supporting Information). After 10000 bending cycles, the capacity retention remained at 82.5%, with no significant fluctuations observed in the GCD curves (Figure 4g).

To evaluate the scalability of the filament battery, an extensive study was conducted. **Figure 5a** demonstrates a near-linear increase in energy output with the length of the filament battery. Additionally, the Voc remains nearly constant with varying lengths (Figure 5b). The performances of the filament battery do not decay as it expands, indicating the promising scalability. This phenomenon can be explained by the hyperbolic tangent function between the filamentary internal polarization resistance and the length,[10b] that is, as the filamentary length increases, the internal polarization resistance decreases before stabilizing. To better understand this relationship, we constructed an equivalent model (Figure 5c). The filament battery can be modeled as consisting of numerous sectional sandwich-structured units, each with a unit length of dx. In this model, the resistance of the core silver current collector is represented by $\rho^{+}dx$, and the resistance of the surficial microscale silver current collector is represented by $\rho^{-}dx$. Under the influence of the salinity gradients and the interfacial redox reactions, ions would transport from rGO to GO as illustrated above. The polarization resistance associated with this process can be expressed as Z/dx, where Z is the polarization resistivity (unit: Ω·m). Resistivity is an inherent property of the material. Once the composition of GO, rGO (thickness, salinity gradient ratio, etc.) and ionic liquids is determined, the Z value is almost constant with the change of fiber length. By applying Ohm's law and solving the equation (Note S1, Supporting Information), the internal polarization resistance (R) of the filament battery at length (L) can be expressed as

$$R = \frac{\left[(\rho^{+} + \rho^{-}) \times Z\right]^{\frac{1}{2}}}{\tan h(kL)} \quad (1)$$

This equation elucidates the hyperbolic cotangent function relationship between internal polarization resistance and fiber length, predicting that the internal polarization resistance will asymptotically approach a stable value as the filamentary length increases. Meanwhile, we also employed COMSOL dynamic simulations to explore this relationship from the perspective of ion diffusion (Figure 5d), given that the internal polarization resistance of the filament battery is directly related to the ion diffusion pathway. The detailed parameters of the COMSOL model are presented in Figure S21 (Supporting Information). Even though the horizontal ionic transport dynamics in GO are several orders of magnitude greater than the vertical ion dynamics (Figure S22, Supporting Information), our simulations reveal that the ion transport pathway remains nanoconfined to specific unit regions under the influence of the electrochemical field. The COMSOL results show that the ions can transport in both vertical and horizontal GO nanoconfined channels in a certain region, where its horizontal transport is limited. This synergetic effect of both vertical and horizontal diffusion was shown to have ultra-high ion transport dynamics due to the reduction of the ion transport energy barrier.[37] This ion transport pathway in specific unit regions prevents ions from diffusing through the horizontal nanoconfined channels of GO over longer distances. The dynamic ion diffusion process is illustrated in Video S4 (Supporting Information). This phenomenon may account for the stabilization of internal polarization resistance beyond a certain filamentary length, as the effective ion transport pathway becomes independent of the length. This result is also consistent with the hyperbolic cotangent function predictions. To validate the applicability of the above theoretical framework to our filament battery, we performed internal polarization resistance measurements by using electrochemical impedance spectroscopy (EIS). As the fiber length was varied from 2 to 50 cm, the Nyquist plot revealed a decrease in the total polarization resistance, which comprises both interfacial and charge transfer resistances (Figure S23a,b, Supporting Information). EIS equivalent circuit fitting results further confirmed that the polarization resistance closely follows a hyperbolic cotangent function trend (Figure 5e). The Z value, derived from the polarization resistance at each length, remained nearly constant despite variations in filament length (Figure S23c, Supporting Information). Finally, to predict the internal polarization resistance by above equation, we measured the conductivities of the core silver current collector and the surficial microscale silver current collector, which were 0.5414 and 0.8439 Ω m^{-1}, respectively. The measured and predicted results of the filament battery showed strong agreement as shown in Figure 5f, corroborating the consistency between theoretical and experimental outcomes.

In addition, we illustrate the reliability of such filament battery in various real-world applications, including wearable/woven electronics, portable healthcare monitors, and all-weather distributed energy management systems. In detail, double 2 cm filament batteries were sufficient to power a commercial calculator driven by ambient humidity (Figure S24 and Video S5, Supporting Information, Beijing 23.0–23.6 °C, 12.1%–20.0% RH). The encapsulated filament battery can be connected in series and integrated with textiles to power watches at least 2 h (Figures S25 and S26 and Video S6, Supporting Information). The textile is also completely waterproof and washable (Figure S27, Supporting Information). Moreover, the filament battery exhibited the capability to harvest solar energy during the day and subsequently power an LED flashlight for ≈10 min at night (Figure 5g). Personalized health management clothing can be rapidly developed by integrating conductive Ag fibers with our filament battery, allowing for seamless incorporation into garments to power

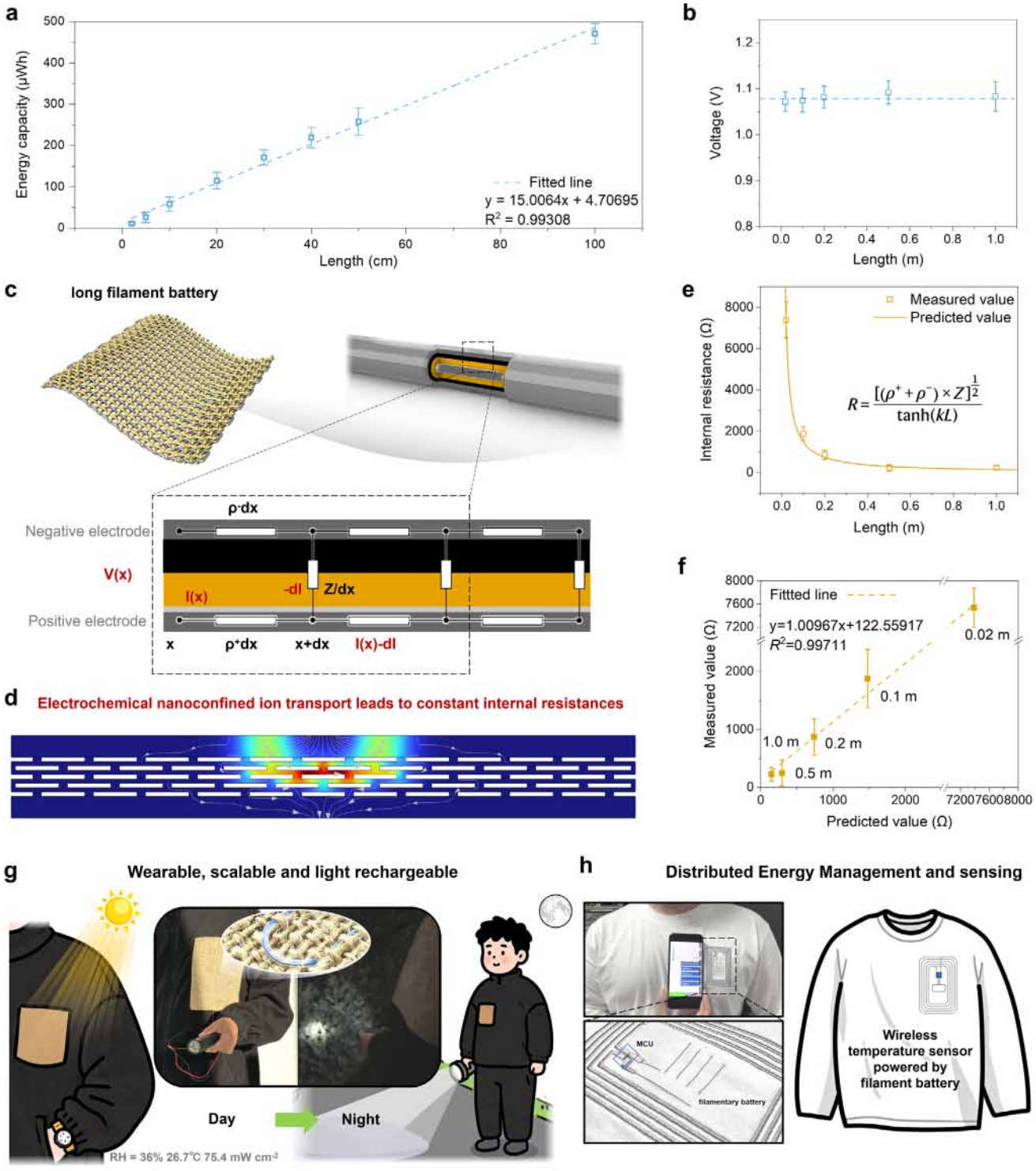

Figure 5. Scalable filament battery for wearable and all-weather DERMS. a) The energy capacity increases linearly with filamentary length, indicating scalability of the energy storage. b) Voltage stability across different filamentary lengths, demonstrating consistent voltage output over a range of lengths up to 1 meter. c) Schematic of long filament battery configuration. d) COMSOL simulation showing electrochemical nanoconfined ion transport along the fiber, contributing to stable internal polarization resistance. e) Comparison of measured and predicted internal polarization resistance values as a function of filamentary length, with good agreement between experimental and theoretical results. f) Fitted line demonstrating the linear relationship between measured internal polarization resistance and predicted values, confirming the reliability of the model over various filamentary lengths. g) Demonstration of the filament battery's wearable, scalable, and light-rechargeable capabilities, with real-world applications for day and night usage. h) Illustration of distributed energy management and sensing system integrated into a wearable garment, showcasing potential for broad-scale wearable electronics.

wearable electronics (Figure 5h; Figures S28 and S29, Supporting Information). This innovative clothing facilitates real-time temperature detection and utilizes Near Field Communication (NFC) to transmit data directly to smartphones (Video S7, Supporting Information). Furthermore, it can integrate circuits for in situ monitoring of critical physiological parameters, functioning as truly disposable and breathable electronics. The efficient and cost-effective production method presents significant potential for early influenza screening, offering a viable strategy to mitigate the widespread transmission of viruses.

3. Conclusion

In conclusion, we have developed the first hair-thin iontronic power source on a single filament for DERMS. This system enables rapid photo-recharging within seconds, facilitated by the design of synergistic photochemical and electrochemical coupling reactions. The controlled ultrasonic spraying technique allows for the seamless integration of stable GO channels on filaments, preserving the integrity of other active layers and facilitating scalability. With a diameter of ≈120 µm, this filament battery (battery thickness ≈10 µm) stands as the world's thinnest rechargeable battery, demonstrating exceptional performance under various conditions and maintaining stability after 10000 bending cycles. The introduction of customized silver halide redox reactions at the electrode surfaces significantly enhances ionic power and energy, yielding gravimetric power densities of 884.95 W kg^{-1} and energy densities of 108.7 Wh kg^{-1}. Our findings confirm a hyperbolic cotangent relationship between internal polarization resistance and filament length, supported by COMSOL dynamic simulations that propose a nanoconfined ion diffusion model. The ultrafine and broad environmental adaptability of this filament battery positions it as a vital component for all-weather energy management, smart textiles, and health monitoring systems. This work lays the groundwork for large-scale energy management solutions on micro- and future nanofibers. Moreover, the coaxial structure with asymmetric electrode areas promotes uniform current distribution based on ionic axial transport pathways, paving the way for future efficient, long-lasting, and compact designs where size and weight are critical.

Supporting Information

Supporting Information is available from the Wiley Online Library or from the author.

Acknowledgements

This work was supported by the Beijing Natural Science Foundation (grant no. IS23040) and National Natural Science Foundation (grant no. 22479016).

Conflict of Interest

The authors declare no conflict of interest.

Data Availability Statement

The data that support the findings of this study are available from the corresponding author upon reasonable request.

Keywords

fiber battery, graphene oxide, Iontronic power source, light rechargeable, nanoconfined channels

Received: November 25, 2024
Revised: February 11, 2025
Published online: March 6, 2025

[1] a) R. Liu, Z. L. Wang, K. Fukuda, T. Someya, *Nat. Rev. Mater.* **2022**, *7*, 870; b) C. J. Traverse, R. Pandey, M. C. Barr, R. R. Lunt, *Nat. Energy* **2017**, *2*, 849; c) A. Facchini, *Nat. Energy* **2017**, *2*, 17129; d) S. Saifi, X. Xiao, S. Cheng, H. Guo, J. Zhang, P. Muller-Buschbaum, G. Zhou, X. Xu, H.-M. Cheng, *Nat. Commun.* **2024**, *15*, 6546.
[2] a) H. Sun, Y. Zhang, J. Zhang, X. Sun, H. Peng, *Nat. Rev. Mater.* **2017**, *2*, 17023; b) Q. Huang, D. Wang, Z. Zheng, *Adv. Energy Mater.* **2016**, *6*, 1600783; c) Y. Gao, C. Xie, Z. Zheng, *Adv. Energy Mater.* **2020**, *11*, 2002838.
[3] A. Libanori, G. Chen, X. Zhao, Y. Zhou, J. Chen, *Nat. Electron.* **2022**, *5*, 142.
[4] a) Z. Sun, Y. Jin, J. Luo, L. Li, Y. Ding, Y. Luo, Y. Qi, Y. Li, Q. Zhang, K. Li, H. Shi, S. Yin, H. Wang, H. Wang, C. Hou, *Nat. Commun.* **2024**, *15*, 8462; b) H. J. Sim, C. Choi, D. Y. Lee, H. Kim, J.-H. Yun, J. M. Kim, T. M. Kang, R. Ovalle, R. H. Baughman, C. W. Kee, S. J. Kim, *Nano Energy* **2018**, *47*, 385.
[5] W. Yang, S. Lin, W. Gong, R. Lin, C. Jiang, X. Yang, Y. Hu, J. Wang, X. Xiao, K. Li, Y. Li, Q. Zhang, J. S. Ho, Y. Liu, C. Hou, H. Wang, *Science* **2024**, *384*, 74.
[6] J. Liang, G. Zhu, C. Wang, Y. Wang, H. Zhu, Y. Hu, H. Lv, R. Chen, L. Ma, T. Chen, Z. Jin, J. Liu, *Adv. Energy Mater.* **2016**, *7*, 1601208.
[7] K. Dong, X. Peng, Z. L. Wang, *Adv. Mater.* **2019**, 32.
[8] S. Li, Y. Li, Y. Shao, H. Wang, *Adv. Fiber Mater.* **2021**, *4*, 129.
[9] a) X. Chen, L. Qiu, J. Ren, G. Guan, H. Lin, Z. Zhang, P. Chen, Y. Wang, H. Peng, *Adv. Mater.* **2013**, *25*, 6436; b) A. B. Dalton, S. Collins, E. Muñoz, J. M. Razal, V. H. Ebron, J. P. Ferraris, J. N. Coleman, B. G. Kim, R. H. Baughman, *Nature* **2003**, *423*, 703.
[10] a) C. Lu, H. Jiang, X. Cheng, J. He, Y. Long, Y. Chang, X. Gong, K. Zhang, J. Li, Z. Zhu, J. Wu, J. Wang, Y. Zheng, X. Shi, L. Ye, M. Liao, X. Sun, B. Wang, P. Chen, Y. Wang, H. Peng, *Nature* **2024**, *629*, 86; b) J. He, C. Lu, H. Jiang, F. Han, X. Shi, J. Wu, L. Wang, T. Chen, J. Wang, Y. Zhang, H. Yang, G. Zhang, X. Sun, B. Wang, P. Chen, Y. Wang, Y. Xia, H. Peng, *Nature* **2021**, *597*, 57.
[11] L. Huang, T. Zhou, S. Zhu, T. Yang, X. Zhou, B. He, S. Wang, W. Yan, L. Wei, *Natl. Sci. Rev.* **2024**, *11*, nwae262.
[12] Q. Chen, S. Sun, T. Zhai, M. Yang, X. Zhao, H. Xia, *Adv. Energy Mater.* **2018**, *8*, 1800054.
[13] Y.-E. Miao, T. Liu, *Adv. Fiber Mater.* **2024**, *6*, 937.
[14] Y. Zhang, Y. Jiao, L. Lu, L. Wang, T. Chen, H. Peng, *Angew. Chem., Int. Ed.* **2017**, *56*, 13741.
[15] a) Y. Zhang, L. Wang, Z. Guo, Y. Xu, Y. Wang, H. Peng, *Angew. Chem., Int. Ed.* **2016**, *55*, 4487; b) L. Ye, X. Cheng, M. Liao, T. Zhao, X. Huang, X. Kang, K. Zhang, X. Sun, B. Wang, H. Peng, *eScience* **2022**, *2*, 606; c) Y. Xu, Y. Zhao, J. Ren, Y. Zhang, H. Peng, *Angew. Chem., Int. Ed.* **2016**, *55*, 7979.
[16] Y. H. Kwon, S. W. Woo, H. R. Jung, H. K. Yu, K. Kim, B. H. Oh, S. Ahn, S. Y. Lee, S. W. Song, J. Cho, H. C. Shin, J. Y. Kim, *Adv. Mater.* **2012**, *24*, 5192.
[17] a) W. Li, J. Zheng, B. Hu, H.-C. Fu, M. Hu, A. Veyssal, Y. Zhao, J.-H. He, T. L. Liu, A. Ho-Baillie, S. Jin, *Nat. Mater.* **2020**, *19*, 1326; b) J. Xu, Y. Chen, L. Dai, *Nat. Commun.* **2015**, *6*, 8103; c) R. Delgado Andrés, R. Wessling, J. Büttner, L. Pap, A. Fischer, B. Esser, U. Würfel, *Energy Environ. Sci.* **2023**, *16*, 5255.

[18] P. Peng, F. Yang, X. Li, S. Li, Z. Wang, D. Wei, *Cell Rep. Phys. Sci.* **2024**, *5*, 101824.
[19] Z. Zhang, L. Wen, L. Jiang, *Nat. Rev. Mater.* **2021**, *6*, 622.
[20] a) P. Peng, F. Yang, Z. Wang, D. Wei, *Adv. Energy Mater.* **2023**, *13*, 2302360; b) L. Yang, F. Yang, X. Liu, K. Li, Y. Zhou, Y. Wang, T. Yu, M. Zhong, X. Xu, L. Zhang, W. Shen, D. Wei, *Proc. Natl. Acad. Sci. U.S.A.* **2021**, *118*, e2023164118; c) D. Wei, *Sci. Rep.* **2015**, *5*, 15173; d) D. Wei, F. Yang, Z. Jiang, Z. Wang, *Nat. Commun.* **2022**, *13*, 4965; e) F. Yang, P. Peng, Z.-Y. Yan, H. Fan, X. Li, S. Li, H. Liu, T.-L. Ren, Y. Zhou, Z. L. Wang, D. Wei, *Nat. Energy* **2024**, *9*, 263.
[21] a) P. Peng, H. Qian, J. Liu, Z. Wang, D. Wei, *Int. J. Smart Nano Mater.* **2024**, *15*, 198; b) T. Emmerich, N. Ronceray, K. V. Agrawal, S. Garaj, M. Kumar, A. Noy, A. Radenovic, *Nat. Rev. Methods Primers.* **2024**, *4*, 69.
[22] S. Kim, S. Choi, H. G. Lee, D. Jin, G. Kim, T. Kim, J. S. Lee, W. Shim, *Nat. Commun.* **2021**, *12*, 47.
[23] J. Liu, N. Wang, L.-J. Yu, A. Karton, W. Li, W. Zhang, F. Guo, L. Hou, Q. Cheng, L. Jiang, D. A. Weitz, Y. Zhao, *Nat. Commun.* **2017**, *8*, 2011.
[24] Y. Xue, Y. Xia, S. Yang, Y. Alsaid, K. Y. Fong, Y. Wang, X. Zhang, *Science* **2021**, *372*, 501.
[25] a) J. Veerman, M. Saakes, S. J. Metz, G. J. Harmsen, *J. Appl. Electrochem.* **2010**, *40*, 1461; b) J. Feng, M. Graf, K. Liu, D. Ovchinnikov, D. Dumcenco, M. Heiranian, V. Nandigana, N. R. Aluru, A. Kis, A. Radenovic, *Nature* **2016**, *536*, 197.
[26] S. C. Abeyweera, K. D. Rasamani, Y. Sun, *Acc. Chem. Res.* **2017**, *50*, 1754.
[27] C. Tang, H. Bai, L. Liu, X. Zan, P. Gao, D. D. Sun, W. Yan, *Appl. Catal. B* **2016**, *196*, 57.
[28] a) C. Zhao, J. Hou, H. Zhang, *Ind. Eng. Chem. Res.* **2023**, *62*, 13734; b) K. Xiao, L. Chen, R. Chen, T. Heil, S. D. C. Lemus, F. Fan, L. Wen, L. Jiang, M. Antonietti, *Nat. Commun.* **2019**, *10*, 74.
[29] a) P. Li, G. Xie, X.-Y. Kong, Z. Zhang, K. Xiao, L. Wen, L. Jiang, *Angew. Chem., Int. Ed.* **2016**, *55*, 15637; b) X. Xie, G. A. Crespo, G. Mistlberger, E. Bakker, *Nat. Chem.* **2014**, *6*, 202.
[30] K. Chen, H. Hu, I. Song, H. B. Gobeze, W.-J. Lee, A. Abtahi, K. S. Schanze, J. Mei, *Nat. Photonics.* **2023**, *17*, 629.
[31] a) Y. Ouyang, X. Li, S. Li, P. Peng, F. Yang, Z. L. Wang, D. Wei, *Nano Energy* **2023**, *116*, 108796; b) P. Peng, P. Shen, H. Qian, J. Liu, H. Lu, Y. Jiao, F. Yang, H. Liu, T. Ren, Z. Wang, D. Wei, *Device* **2024**, *3*, 100574.
[32] K. Sivula, R. van de Krol, *Nat. Rev. Mater.* **2016**, *1*, 15010.
[33] K. A. Mauritz, R. B. Moore, *Chem. Rev.* **2004**, *104*, 4535.
[34] N. Dombrowski, W. R. Johns, *Chem. Eng. Sci.* **1963**, *18*, 203.
[35] G. Li, Z. Liu, Q. Huang, Y. Gao, M. Regula, D. Wang, L.-Q. Chen, D. Wang, *Nat. Energy* **2018**, *3*, 1076.
[36] S. Kondrat, P. Wu, R. Qiao, A. A. Kornyshev, *Nat. Mater.* **2014**, *13*, 387.
[37] Z. Man, J. Safaei, Z. Zhang, Y. Wang, D. Zhou, P. Li, X. Zhang, L. Jiang, G. Wang, *J. Am. Chem. Soc.* **2021**, *143*, 16206.